Understanding lithium-ion transport in selenophosphate-based lithium argyrodites and their limitations in solid-state batteries

Johannes Hartel,¹ Ananya Banik,¹ Josef Maximilian Gerdes,² Björn Wankmiller,^{2,3} Bianca Helm,¹ Cheng Li,⁴ Marvin Kraft,⁵ Michael Ryan Hansen,² Wolfgang G. Zeier^{1,5*}

¹Institute of Inorganic and Analytical Chemistry, University of Münster, Corrensstrasse 28/30, 48149 Münster, Germany

²Institute of Physical Chemistry, University of Münster, Corrensstrasse 28/30, 48149 Münster, Germany

³International Graduate School BACCARA, Wilhelm-Schickard-Straße 8, 48149 Münster, Germany

⁴Neutron Scattering Division, Oak Ridge National Laboratory (ORNL), Oak Ridge, Tennessee 37831-6473, United States

⁵Institut für Energie- und Klimaforschung (IEK), IEK-12: Helmholtz-Institut Münster, Forschungszentrum Jülich, Corrensstrasse 46, Münster 48149, Germany

*wzeier@uni-muenster.de

Abstract

To develop solid-state batteries with high power and energy densities, solid electrolytes with fast Li⁺ transport are required. Superionic lithium argyrodites have proven to be a versatile system, in which superior ionic conductivities can be achieved by elemental substitutions. Herein, report the novel selenophosphate-based lithium we $\text{Li}_{6-x}\text{PSe}_{5-x}\text{Br}_{1+x}$ ($0 \le x \le 0.2$) exhibiting ionic conductivities up to 8.5 mS·cm⁻¹ and uncover the origin of their fast Li⁺ transport. Rietveld refinement of neutron powder diffraction data reveals a better interconnection of the Li⁺ cages compared to the thiophosphate analogue Li₆PS₅Br, by occupation of two additional Li⁺ sites, facilitating fast Li⁺ transport. Additionally, a larger unit cell volume, lattice softening and higher structural disorder between halide and chalcogenide are unveiled. The application of Li_{5.85}PSe_{4.85}Br_{1.15} as catholyte in In/LiIn|Li₆PS₅Br| LiNi_{0.83}Co_{0.11}Mn_{0.06}O₂:Li_{5.85}PSe_{4.85}Br_{1.15} solid-state batteries leads to severe degradation upon charging of the cell, revealing that selenophosphate-based lithium argyrodites are not suitable for application in lithium nickel cobalt manganese oxide (NCM) based solid-state batteries from a performance perspective. This work further expands on the understanding of the structuretransport relationship in Li⁺ conducting argyrodites and reemphasizes the necessity to consider chemical and electrochemical stability of solid electrolytes against the active materials when developing fast Li⁺ conductors.

1. Introduction

Solid-state Li-metal batteries provide a promising alternative to state-of-the-art liquid electrolyte-based batteries to improve safety and performance.^{1–3} Solid electrolytes are the centerpiece of solid-state batteries, which can be used as separator and to provide sufficient ionic percolation in composite cathodes (as catholyte) or composite anodes (as anolyte).^{4,5} To realize sufficient areal loadings of active material for competitive energy densities, solid electrolytes with ultrafast Li⁺ transport are one major requirement.^{5–8}

A plethora of Li⁺ conducting materials have been developed as solid electrolytes for solid-state batteries including oxides^{9,10}, halides^{11–13}, phosphates^{14–16} and thiophosphates^{17–21}. Among these materials, lithium thiophosphates stand out owing to their high ionic conductivities and mechanical softness.^{17,19–22} Especially, the lithium argyrodites Li₆PS₅X (X = Cl, Br, I) have recently attracted significant attention²³, since some of the fastest Li⁺ conductors can be synthesized by elemental substitution of these materials, including Li_{6.6}P_{0.4}Ge_{0.6}S₅I ($18.4 \pm 2.7 \text{ mS} \cdot \text{cm}^{-1}$)¹⁷ and Li_{6.6}Si_{0.6}Sb_{0.4}S₅I ($24 \text{ mS} \cdot \text{cm}^{-1}$)²⁴. At this point, there are a variety of compositions that exhibit ionic conductivities above 10 mS·cm⁻¹,^{17,18,24–26} which is indeed the necessary ionic conductivity to provide fast enough transport in composite electrodes.²⁷

Lithium argyrodites can crystallize in a low-temperature orthorhombic and a high-temperature cubic polymorph, of which only the cubic polymorph in space group $F\overline{4}3m$ is a superionic conductor. While the phase transition temperature strongly depends on the exact composition, the halide incorporation has been found to be crucial for stabilization of the high-temperature polymorph at room temperature. In the fully-ordered crystal structure of cubic Li_6PS_5X , which is exemplary as shown in Figure 1a, the halide anions X form a face-centered cubic lattice (Wyckoff 4a) with the octahedral voids occupied by PS_4^{3-} tetrahedra (P on Wyckoff 4b and S on Wyckoff 16e) and free sulfide on half of the tetrahedral sites (Wyckoff 4d). However, for $X = \text{Cl}^-$ and Br^- there is X'/S^{2-} site-disorder between Wyckoff 4a and Wyckoff 4d, which can be further tuned by adjusting the synthesis conditions. By altering the composition, it seems that site-disorder can even be induced in the case of the iodide-materials. Computational and experimental studies suggest that the site-disorder is promoted by similar ionic radii of S^{2-} and $X^{-32,36}$

There is a strongly positive correlation between site-disorder and enhanced Li⁺ transport, which has been linked to an improved interconnection of the Li⁺ substructure through occupation of new Li⁺ sites in site-disordered structures.^{35,37,38} Generally, there are five types of tetrahedral voids in the lithium argyrodites structure that can potentially be occupied by lithium ions, classified as type 1 to type 5 (T1 to T5) based on the number of corners and edges shared by each tetrahedron with neighboring PS₄³⁻ units as illustrated in Figure S1.^{31,38} While for Li₆PS₅I only type 5 positions (T5 and T5a) have been reported, recent crystallographic studies have

revealed an additional partial occupation of the T2 position for Li₆PS₅Cl and Li₆PS₅Br.³⁷ Occupancy on these positions results in cage-like Li⁺ structures around the Wyckoff 4*d* site. This strongly affects the ionic transport properties, since different Li⁺ jump processes can occur depending on the occupied tetrahedral Li⁺ positions.^{38,39} When only type 5 sites are occupied, as it is the case for Li₆PS₅I, Li⁺ transport is restricted to localized doublet-jumps T5-T5a-T5 from the center of one T5 tetrahedron via a shared tetrahedral face (T5a, 24*g*) that do not form an interconnected network for three-dimensional transport. With additional Li⁺ occupancy on T2 positions, inter-cage Li⁺ transport via T5-T2-T2-T5 is facilitated as shown in Figure 1b, resulting in significantly improved ionic conductivities of over three orders of magnitude for Li₆PS₅Cl and Li₆PS₅Br compared to Li₆PS₅I.^{32,37} In some "Li⁺ excess" systems with x(Li) > 6 including Li_{6.6}P_{0.4}Ge_{0.6}S₅I, Li⁺ occupancy on T4 positions has been reported suggesting that even faster transport can be achieved if this position is occupied.³⁵ First-principles molecular dynamics calculations have revealed that the occupancy on this site opens up another low-energy inter-cage diffusion pathway via T5-T4-T5, contributing to the ultrafast Li⁺ conduction of Li_{6.6}P_{0.4}Ge_{0.6}S₅I.³⁸

Recently, an increasing halogen content has been found to significantly improve the ionic transport in $\text{Li}_{6-x}\text{PS}_{5-x}\text{Cl}_{1+x}^{18,28}$ and $\text{Li}_{6-x}\text{PS}_{5-x}\text{Br}_{1+x}^{26}$ solid solutions with reports of ionic conductivities up to 12 mS·cm⁻¹ and 11 mS·cm⁻¹, respectively for sintered pellets along with significantly decreased activation barriers. Gautam *et al.* have correlated the improved ionic conductivity of $\text{Li}_{6-x}\text{PS}_{5-x}\text{Cl}_{1+x}$ with the lowering of the effective anionic charge by introducing an excess of chloride in the Li⁺ cage center. ²⁸ By presence of monovalent anions on Wyckoff 4*d* sites, the Coulomb interactions between the central anion and lithium ions are weakened. This results in an increased mean distance of lithium ions from the cage center (R_{mean}), which in turn facilitates inter-cage transport as a consequence of smaller inter-cage distances and thus decreased activation barriers. ^{28,33,34} Similar influences of the descriptor R_{mean} has been found in $\text{Li}_{6-6}\text{Po}_{4}\text{Geo}_{6}\text{S}_{5}\text{I}$ as well. ³⁵

Inspired by the previous success of introducing an excess of halide into the argyrodite structure, we have investigated the effect of introducing excess bromide into selenophosphate-based argyrodites of the Li_{6-x}PSe_{5-x}Br_{1+x} solid solution series. Based on reports on Li₆PS_{5-x}Se_xBr⁴⁰ and Li₆PS_{5-x}Se_xI⁴¹ the introduction of larger and more polarizable Se²⁻ is expected to lead to widening of diffusion pathways and lattice softening, which is expected to further improve ionic transport. Structural changes, including changes in the Li⁺ substructure, have been investigated by high-resolution powder neutron diffraction and ³¹P MAS NMR. The ionic transport properties are explored by temperature dependent impedance spectroscopy and ⁷Li nuclear magnetic resonance spin-lattice relaxometry. This work shows that the ionic conductivity can increased 8.5 mS⋅cm⁻¹ by increasing the bromide content Li_{6-x}PSe_{5-x}Br_{1+x} solid solution series. Compared to previously reported Li₆PS₅Br, the selenophosphate-based Li_{6-x}PSe_{5-x}Br_{1+x} substitution series reveals larger lattice parameters and lower activation energies for Li⁺ transport, coupled with a higher degree of Se²⁻/Br⁻ sitedisorder. The substitution has significant effects on the Li^+ substructure, leading to the occupation of two additional Li^+ positions, T4 and T3, which offer additional pathways for inter-cage Li^+ diffusion when compared to Li_6PS_5Br . Finally, the novel fast-conducting bromide-rich selenophosphate $Li_{5.85}PSe_{4.85}Br_{1.15}$ is tested as a catholyte in solid-state batteries and compared to the sulfide-based Li_6PS_5Br , demonstrating that even if fast ionic transport is achieved, stability and usability of the solid electrolytes in solid-state batteries is not always a given.

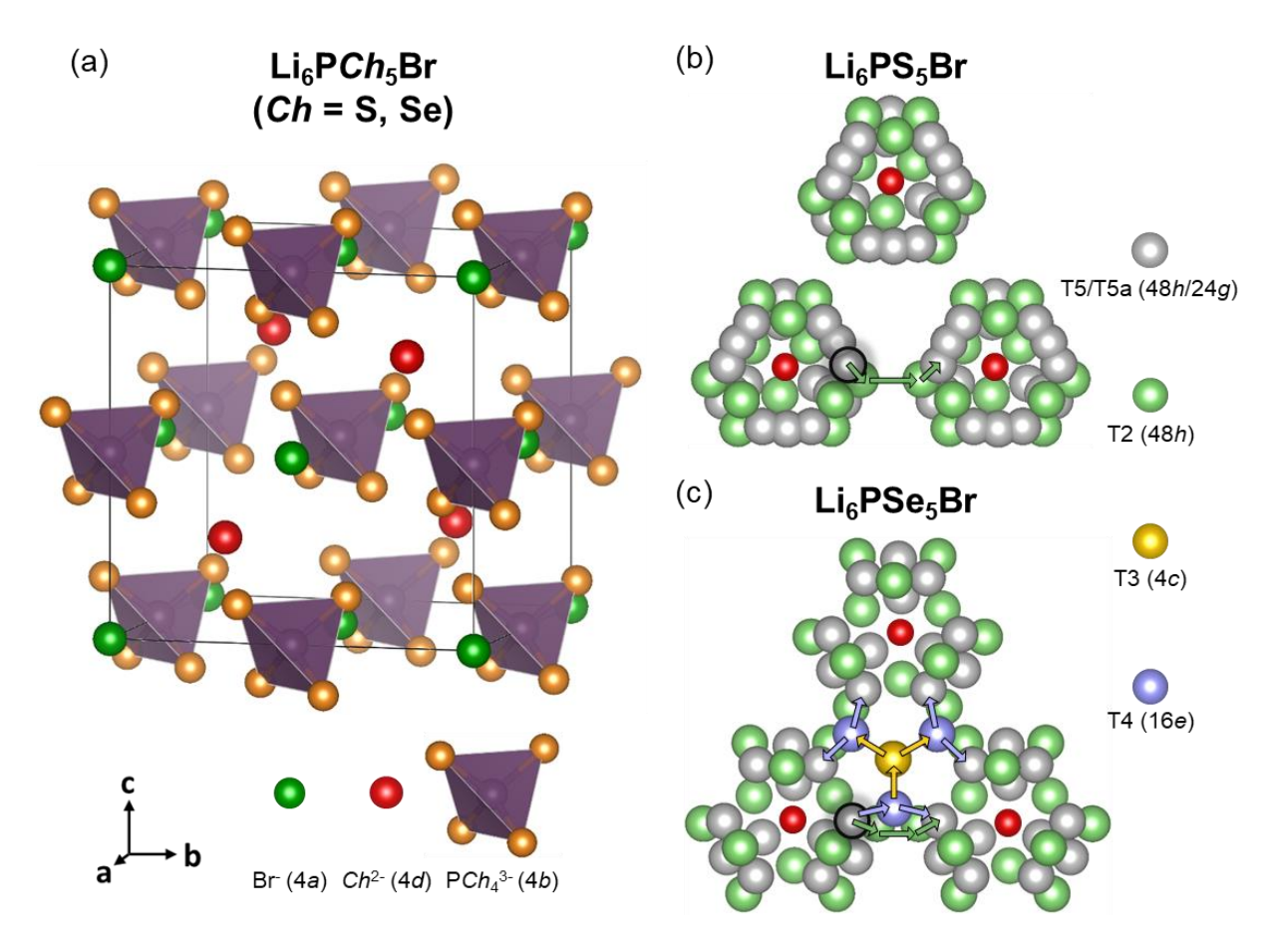


Figure 1. (a) Unit cell of Li_6PCh_5Br (Ch = S, Se) in the anion-ordered configuration. Br^- ions form a face-centered cubic structure with Ch^{2-} occupying half of the tetrahedral voids and PS_4^{3-} units occupying the octahedral interstices. Introduction of larger selenides leads to expansion of the unit cell volume. The Li^+ cages around the Wyckoff 4d position are excluded for the sake of clarity. (b) Li^+ cages around the Wyckoff 4d position in Li_6PS_5Br include type 5 and type 2 Li^+ positions, which only enables inter-cage jumps via T2 sites. The arrows describe Li^+ transport pathways from one T5 position to T5 positions of neighboring Li^+ cages. (c) Li^+ cages around the Wyckoff 4d position in Li_6PSe_5Br include type 5, type 2, type 3 and type 4 Li^+ positions, which enables multiple inter-cage jump pathways. The arrows describe potential Li^+ transport pathways from one T5 position to T5 positions of neighboring Li^+ cages.

2. Experimental

Synthesis. All syntheses of the Li_{6-x}PSe_{5-x}Br_{1+x} substitution series ($0 \le x \le 0.25$) were carried out in a glovebox under argon atmosphere (H₂O < 0.1 ppm, O₂ < 0.1 ppm). Lithium bromide (*Alfa Aesar*, 99.998%), selenium (*Alfa Aesar*, 99.999%), red phosphorus (*ChemPUR*, 99.99%) and freshly prepared lithium selenide (as described below) were mixed in stochiometric ratio. The mixtures were hand ground in an agate mortar, pressed into pellets and filled into carbon coated quartz ampules with an inner diameter of 10 mm and 10-12 cm length, which were then sealed under vacuum. All ampoules were dried for two hours at 800 °C under dynamic vacuum p < 4 mbar prior to their use to ensure the absence of any water in the reaction atmosphere. The sealed ampoules were then transferred into a tube furnace and heated to 450 °C at a heating rate of 100 °C/h followed by further two weeks of annealing at 450 °C. The final product was obtained after air-quenching and the obtained pellets were hand ground for further characterization. All powders were kept under argon atmosphere or vacuum at all times to prevent contact with moisture and oxygen.

The precursor lithium selenide was prepared via the stochiometric reaction of selenium powder (*Alfa Aesar*, 99.99%) and elemental lithium (*Alfa Aesar*, 99.9%). First, selenium powder was transferred into a quartz ampule with an inner diameter of 12 mm and 10-12 cm length, which was pre-dried as described above. Then, elemental lithium was weighed into a graphite crucible, which was pre-dried together with the quartz ampoule. Subsequently, the graphite crucible containing elemental lithium was placed in the same ampoule. The ampoule was cooled in liquid nitrogen to prevent sublimation of selenium, was sealed under vacuum, transferred into a tube furnace and heated from room temperature to 400 °C at a rate of 12 °C/h, followed by 48 h of annealing. After natural cooling, lithium selenide was obtained, which was hand ground and checked for purity by powder X-ray diffraction before use.

Neutron powder diffraction. Neutron powder diffraction data of the Li_{6-x}PSe_{5-x}Br_{1+x} ($0 \le x \le 0.4$) samples were collected at Oak Ridge spallation neutron source (SNS, Oak Ridge National Laboratory) using the PAC automatic sample changer at the POWGEN diffractometer (BL-11A beamline). The samples (~600 mg) were placed into cylindrical vanadium cans (\emptyset = 3 mm) and sealed with a copper gasket under inert atmosphere to avoid air exposure during the measurement. The diffraction data were collected for seven hours per diffractogram in high-resolution mode with a center wavelength of 1.5 Å. All samples were measured at 293 K. Additionally, diffraction data was collected for two selected compositions, Li₆PSe₅Br and Li_{5.85}PSe_{4.85}Br_{1.15}, at 250 K, 200 K and 150 K. The comparison of the structural data to Li₆PS₅Br is based on previous work by Minafra *et al.* using the same instrument and conditions.³⁷

Rietveld analysis. Rietveld refinements were carried out on absorption-corrected neutron diffraction data using the TOPAS-Academic V6 software package. The structural model by Minafra *et al.* obtained from neutron refinements of Li₆PS₅Br was used as starting model.³⁷ Pseudo-Voigt and GSAS back-to-back exponential functions were used to fit the peak profile

shape. Strategies assessed based on the indicators R_{wp} and goodness of fit (GOF). Following parameters were refined in the given order: (1) Scale factor, (2) background fit by a Chebychev polynomial with 12 parameters, (3) lattice parameter and (4) the peak shape. Once a suitable profile fit was achieved, the (5) isotropic thermal displacements parameters, (6) fractional atomic coordinates and (7) occupancies were refined for all elements except for lithium. Finally, Li⁺ positions were investigated. All possible Li⁺ positions including T1-T5 and T5a were probed during refinement, using the starting conditions from Minafra *et al.* Once negative or unphysical values for displacement parameters or occupancies occurred the occupancy of lithium on the corresponding sites was assumed to be below the resolution limit and was thus not included into the refinement model. The occupancy of Li⁺ positions was constrained to maintain the nominal stoichiometry and thereby ensure charge neutrality. Additionally, the same displacement parameter for all Li⁺ positions was assumed due to their similar chemical environment in tetrahedral coordination, and this was needed for a stable refinement. All constraints applied during the Rietveld refinements as well as the results of the refinements are given in Tables S1 to S12.

Raman spectroscopy. The samples were fixed on a microscopy glass slide using Kapton tape to prevent reactions with humidity and ambient air. For the measurements, a Bruker Senterra II Raman microscope with a laser wavelength of 532 nm and a laser power of 2.5 mW was used. Each sample was measured at four different positions applying a 20-fold magnification lens and an integration time of 5 s. The Raman spectra were recorded in a 47-1548 cm⁻¹ range with a spectral resolution of 4 cm⁻¹. For data processing the *OPUS* 7.5 software package was used.

Potentiostatic electrochemical impedance spectroscopy. AC impedance spectroscopy was applied to determine the ionic conductivities. Approximately 300 mg of the powders were hand pressed into pellets, which were then isostatically pressed at 413 MPa for 30 minutes. The obtained pellets were put into 10-12 cm long, carbon coated quartz glass ampoules with an inner diameter of 10 mm. After sealing the ampoules under vacuum, the pellets were placed in a tube furnace and sintered at 450 °C for ten minutes, followed by natural cooling, resulting in relative densities between 89% - 95%. Due to its higher fragility under natural cooling conditions a cooling rate of 10 °C/h was used for the pellet with the nominal composition Li_{5.8}PSe_{4.8}Br_{1.2}. All pellets were then sputter coated with gold electrodes under vacuum of 0.1 mbar, using a sputtering time of 300 s per side and a current of 30 mA. Subsequently, the pellets were incorporated into a pouch cell with dimensions of ~2 cm × 2 cm and contacted using aluminum current collectors. The impedance spectra were recorded with an Alpha-A impedance analyzer (Novocontrol Technologies) in a temperature range from 298 K to 173 K. An AC excitation voltage of 10.6 mV was applied to record spectra in a frequency range of 5 MHz to 100 mHz. Before each measurement, the temperature was equilibrated for one hour to ensure the sample has reached the targeted temperature. For further evaluation of the data, including the fitting of the Nyquist plots, the RelaxIS 3 software package by rhd instruments was used. The data quality was assessed by Kramer-Kronigs analysis to determine the reliable frequency range for fitting of the data. Uncertainties of the ionic conductivity were calculated from fit and geometrical errors.

Nuclear magnetic resonance (NMR) spectroscopy. Solid-state 31 P magic-angle spinning (MAS) NMR spectra were recorded on a Bruker DSX 500 spectrometer equipped with a 11.74 T wide bore magnet using a 2.5 mm Bruker MAS probe operating at a Larmor frequency of 202.4 MHz. A pulse length of 2.5 μ s, corresponding to a flip angle of π /2 at a nutation frequency of 100 kHz, and a recycle delay of 100 s were used for the single-pulse excitation scheme. The powder samples were packed into 2.5 mm ZrO₂ rotors under argon atmosphere. MAS was conducted at a rotation frequency of 25.0 kHz and the magic angle was calibrated using the 23 Na resonance of solid NaNO₃ under MAS. The 31 P chemical shift scale was referenced to phosphoric acid (H₃PO₄) at 0 ppm.

Static saturation-recovery ^7Li NMR experiments were recorded on a Bruker Avance III 300 spectrometer equipped with a 7.05 T wide bore magnet using a VTN broadband probe operating at a Larmor frequency of 116.6 MHz. The powder samples were transferred into 4 mm ZrO₂ rotors under argon atmosphere. All experiments were conducted with a pulse length of 2.5 µs for a flip angle of π /2, corresponding to a nutation frequency of 100 kHz. The length of the recovery delay was incremented with four steps per decade from $t_1 = 10^{-5}$ s to $t_{28} = 56.234$ s. The free-induction decays were Fourier transformed and integrated in TopSpin and the resulting signal intensity curves were fitted using an exponential saturation function with stretching exponent. The temperature of the sample was regulated in the temperature range between 200 K and 290 K by using a nitrogen gas flow of an Air Jet XR compressor-based cooling system from SP Scientific (FTS Systems) and electrical heating. In the temperature range from 320 K to 440 K an uncooled nitrogen gas flow and electrical heating were used to stabilize the temperature. External calibration of the temperature was achieved by using the chemical shift differences of the 1 H NMR resonances of methanol (200 K to 290 K) and ethylene glycol (320 K to 440 K).

Assembly of solid-state batteries. To compare the performance of Li_{5.85}PSe_{4.85}Br_{1.15} as catholyte Li₆PS₅Br, solid-state battery half-cells of the composition In/LiIn | Li₆PS₅Br | NCM83:Li_{5.85}PSe_{4.85}Br_{1.15} and In/LiIn | Li₆PS₅Br | NCM83:Li₆PS₅Br were assembled in press cells in a glovebox under argon atmosphere ($H_2O < 0.1$ ppm, $O_2 < 0.1$ ppm). The setup of the press cells is adapted from a previous report.⁴⁴ Commercial LiNi_{0.83}Co_{0.11}Mn_{0.06}O₂ (NCM-83, MSE supplies) was dried over night at 250 °C in a Büchi B-585 glass oven prior to use. For the composite cathode, the as-prepared Li_{5.85}PSe_{4.85}Br_{1.15} and Li₆PS₅Br were used as catholyte and NCM-83 was used as the cathode active material. While NCM-83 and Li_{5.85}PSe_{4.85}Br_{1.15} were weighted in a 54:46 weight ratio, NCM-83 and Li₆PS₅Br were weighted in a 65:35 weight ratio to obtain a 45:55 volume ratio in both cases. The mixtures were subsequently soft milled in a 100 mg batch for 15 minutes at 15 Hz using five ZrO₂ balls ($\emptyset = 5$ mm). For the cell assembly, 60 mg of Li₆PS₅Br was filled

into the press cell as separator. After hand pressing, 12 mg of the cathode composite was distributed homogeneously on the separator surface. Subsequently, a pressure of three tons was applied for three minutes. For the anode a lithium rod (abcr, 99.8%) was cut into 1.5-2 mg pieces and pressed into foil. The freshly prepared lithium foil and indium foil (chemPUR, 100 µm thickness, 9 mm diameter, 99.999%) were used to form the In/LiIn anode in-situ. After finishing the cell assembly, the press cells were fixed in an aluminum frame and put under ~60 MPa pressure. Before starting electrochemical measurements, the battery was rested at OCV for six hours to allow for formation of the In/LiIn alloy and to achieve microstructural relaxation. For cell cyclisation, the cells were charged to 3.7 V and discharged to 2.0 V versus In/LiIn at 298 K using a C-rate of 0.1 C based on a capacity of 200 mAh·g_{CAM}⁻¹ for NCM-83. To investigate the influence of applied potential on the degradation during cycling, half-cells were charged with 0.1 C from 2.0 - 3.7 V versus In/LiIn in steps of 0.2 V. After each charging step the batteries were rested for one hour, followed by a potentiostatic electrochemical impedance spectroscopy (PEIS) measurement. Those PEIS measurements were performed at 298 K using a BioLogic VMP-300 potentiostat. An AC voltage of 10 mV was applied and impedance spectra were recorded in a frequency range of 7 MHz to 10 mHz. For further evaluation of the data, including the fitting of the Nyquist plots, the RelaxIS 3 software package by rhd instruments was used. The data quality was assessed by Kramer-Kronigs analysis to determine the reliable frequency range for fitting of the data.

3. Results & Discussion

Structural characterization. Lithium argyrodites of the target composition $\text{Li}_{6-x}\text{PSe}_{5-x}\text{Br}_{1+x}$ (x=0,0.05,0.1,0.15,0.2, and 0.3) have been synthesized with increasing bromide content, to assess the influence of structural changes on ionic transport properties and were checked for purity using powder X-ray diffraction. For the structural characterization, neutron powder diffraction has been carried out, and the diffraction patterns were analyzed by Rietveld refinement. In contrast to X-ray diffraction, neutron diffraction data allows to differentiate between the isoelectronic bromide and selenide and further enables detailed investigation of the Li^+ substructure. All neutron diffraction patterns are shown in Figure S2.

For the $\text{Li}_{6-x}\text{PS}_{5-x}\text{Cl}_{1+x}$ solid solution series a certain solubility limit exists and the free S²- cannot be fully replaced by the halide anion. Here, in the case of $\text{Li}_{6-x}\text{PSe}_{5-x}\text{Br}_{1+x}$, a sharp increase of a LiBr side-phase is observed at x=0.3 by powder neutron diffraction data (Figure S3) suggesting that the solubility limit is reached between 0.2 < x < 0.3. All compositions within the solid solution regime only contain a minimal amount of LiBr side phase below 2 wt% and therefore close to the detection limit and no further side phases were observed. Investigation of the lattice parameter by Rietveld refinement against the neutron diffraction data reveals a linear decrease of the lattice parameter up to x=0.2 (Figure 2a). Potential explanations for the unit cell contraction are the increase in Li^+ vacancy content or changes in the Li^+ substructure as

observed in Li_{6-x}PS_{5-x}Cl_{1+x}. ²⁸ Since the ionic radii of Se²⁻ (1.96 Å) and Br⁻ (1.98 Å) are similar⁴⁵, this should only have negligible influence on the lattice parameter. Beyond x = 0.2, no further decrease of the lattice parameter is observed, supporting above findings regarding the solubility limit. Due to the onset of side-phase for compositions with x > 0.2, only the compositions $0 \le x \le 0.2$ were considered for all further investigations.

For the refinement of the neutron diffraction data, the structural model from Minafra et al. for Li₆PS₅Br was used as starting point.³⁷ The refinement data of all compositions and employed constraints, including tabulated structural data are compiled in the Supporting Information (Figures S4, S5 and Tables S1-S12). All compositions crystallize in cubic $F\overline{4}3m$ space group, typical for the fast-conducting lithium argyrodite high-temperature polymorph. The full replacement of S²⁻ in Li₆PS₅Br by larger Se²⁻ as in Li₆PSe₅Br leads to significant expansion of the unit cell volume, indicated by an increasing lattice parameter a (Figure 2a). Additionally, a higher site-disorder between the chalcogenide and halide is observed for Li₆PSe₅Br when compared to Li₆PS₅Br, possibly due to the larger size-mismatch between S²⁻ and Br⁻, compared to Se²⁻ and Br⁻ (Figure 2b). While the Br⁻/Ch²⁻ site-disorder for pristine Li₆PS₅Br is 16.1(6)%, the site-disorder is 44.7(7)% in the case of Li₆PSe₅Br, leading to a significantly higher halide occupancy on the Wyckoff 4d position. For increasing degrees of substitution x in Li_{6-x}PSe_{5-x}Br_{1+x}, Rietveld refinement of the powder neutron diffraction data reveals a steady increase of Br occupancy on Wyckoff 4d from 44.7(7)% for x = 0 up to 50.2(7)% for x = 0.2. To further probe the Br⁻ site occupation of Wyckoff 4d in the Li_{6-x}PSe_{5-x}Br_{1+x} substitution series, ³¹P MAS NMR spectra have been recorded for compositions with x = 0 to 0.2, as exemplary shown for Li₆PSe₅Br in Figure 2c and for all remaining compositions in Figure S6. As described by Koch et al. 46 and comparably for the Li₆PS₅Br by Wang et al. 26, the mixed Wyckoff 4d site occupation by Br-/Se²⁻ splits the ³¹P NMR resonance into five signals in the range of -75.6 to -98.5 ppm. They can be assigned according to a distribution of Br⁻/Se²⁻ on the four nearest neighbor Wyckoff 4d positions around the PSe₄³⁻ tetrahedron with (in order of decreasing chemical shift) 4Se, 3Se1Br, 2Se2Br, 1Se3Br and 4Br as illustrated in Figure S7. From the relative integrals of each ³¹P signal, the bromide occupation on Wyckoff 4d can be compared to the results from the neutron diffraction data in Figure 2d. In agreement with the results from neutron powder diffraction, a trend towards higher Br occupation of the Wyckoff 4d position with an increasing degree of substitution x was found. The Br occupancy from ³¹P MAS NMR measurements can be given as 45.3(5)% in the case of Li₆PSe₅Br and steadily increases to 51.1(5)% in the case of x = 0.2 for $\text{Li}_{6-x}\text{PSe}_{5-x}\text{Br}_{1+x}$. With probabilities for a statistical mixing taken from the relative integral analyses, the Br and Se²⁻ site-occupancy on Wyckoff 4d can be modeled with a binomial distribution, as shown in Figure S8. Comparing the relative integrals from ³¹P MAS NMR to the binomial model, the most apparent difference is the lower-than-expected occurrence of 4Br and 4Se-coordinated PSe₄³⁻ tetrahedra, which could be explained by a preference towards homogeneous charge distribution in close proximity to the PSe₄³- tetrahedra. The presence of PSe₄³- tetrahedra was verified by Raman spectroscopy.

For all compositions of the $\text{Li}_{6-x}\text{PSe}_{5-x}\text{Br}_{1+x}$ substitution series the symmetric stretching mode of PSe_4^{3-} tetrahedra is observed at wavenumbers $v = 233 - 235 \text{ cm}^{-1}$, which is in line with previous reports (Figure S9). According to Bernges *et al.* the wavenumber of the symmetric stretching mode of the PS_4^{3-} units in $\text{Li}_6\text{PS}_5\text{Br}$ lies at $v = 420 \text{ cm}^{-1}$, indicating softening of the lattice upon full substitution of S^{2-} by Se^{2-} . Besides purely static structural influences on ionic conductivity such as Li^+ concentration and width of diffusion pathways, the dynamics of the host lattice have been shown to strongly impact ionic transport. Here, the softer anion sublattice incorporating Se^{2-} aids fast ion conduction, since it exhibits a weaker bonding interaction to the mobile lithium ions.

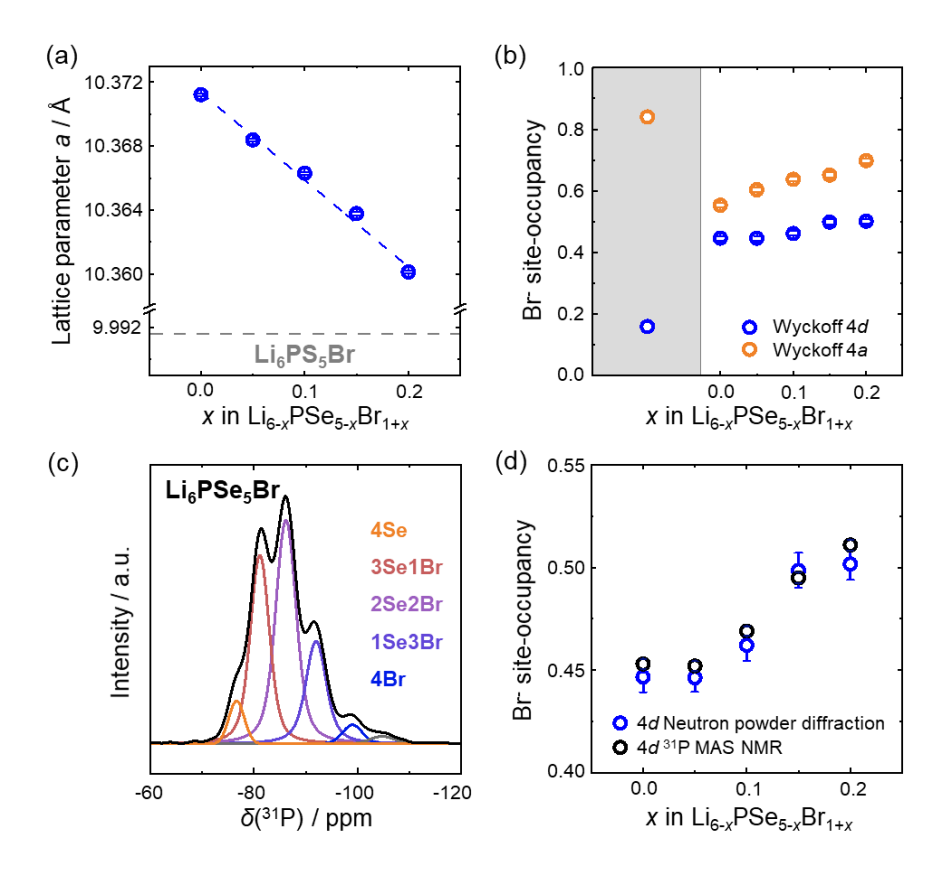


Figure 2. (a) The lattice parameter decreases linearly along with increasing degree of substitution. (b) The evolution of bromide occupancy along with increasing degree of substitution. (c) ³¹P MAS NMR spectrum of Li₆PSe₅Br showing the spectral deconvolution and assignment with respect to the occupancy of the Wyckoff 4d positions (see Figure S7 for details). (d) ³¹P MAS NMR and neutron powder diffraction data show a trend towards higher bromide site-occupancy on Wyckoff 4d with an increasing degree of substitution. The uncertainties correspond to one standard deviation based on the refinement of the neutron powder diffraction data.

For the Rietveld refinement of the powder neutron diffraction data all tetrahedrally coordinated positions that can possibly be occupied by lithium ions (T1-T5) were considered. Thereby, nonnegligible occupancies on four Li⁺ positions including T5, T2, T4 and T3 are found. The Li⁺ occupancies found for Li_{6-x}PSe_{5-x}Br_{1+x} and previously reported for Li₆PS₅Br by Minafra *et al.*

are shown in Figure 3a. Compared to the Li⁺ substructure of Li₆PS₅Br, there is a significantly higher Li⁺ occupancy on the T2 site for all investigated Li_{6-x}PSe_{5-x}Br_{1+x} compositions. While for Li₆PS₅Br approximately 30% of all lithium ions occupy T2 sites, this share lies at 48(2)% for Li₆PSe₅Br and steadily increases up to 55(2)% for Li_{5.8}PSe_{4.8}Br_{1.2}. Additionally, all compositions of Li_{6-x}PSe_{5-x}Br_{1+x} show occupancy on the T4 site (between 2.9(9)% and 3.9(10)%) and the T3 site (between 3.2(5)% and 3.7(4)%) which have not been reported for Li₆PS₅Br. Occupancy on the T4 site has previously been found for highly conducting Li_{6+x}P₁₋ _xGe_xS₅I solid solutions³⁵ and is hypothesized to open up an additional pathway for inter-cage Li⁺ diffusion.³⁸ Occupancy on the T3 site has also been reported for high conducting thioantimonate-based lithium argyrodites.²⁴ The occupancy on type 5 positions is reduced to around 40% as opposed to approximately 70% in the case of Li₆PS₅Br. In general, all studied compositions of Li_{6-x}PSe_{5-x}Br_{1+x} exhibit a significantly higher occupancy of positions involved in inter-cage transport i.e. T2, T4 and T3. These results suggest that the Li⁺ cages are more interconnected than for Li₆PS₅Br, facilitating long-range Li⁺ transport as illustrated in Figure 3c,d. Increasing occupation of the T2 position with increasing degree of substitution suggests that with higher x the preference towards inter-cage transport increases.

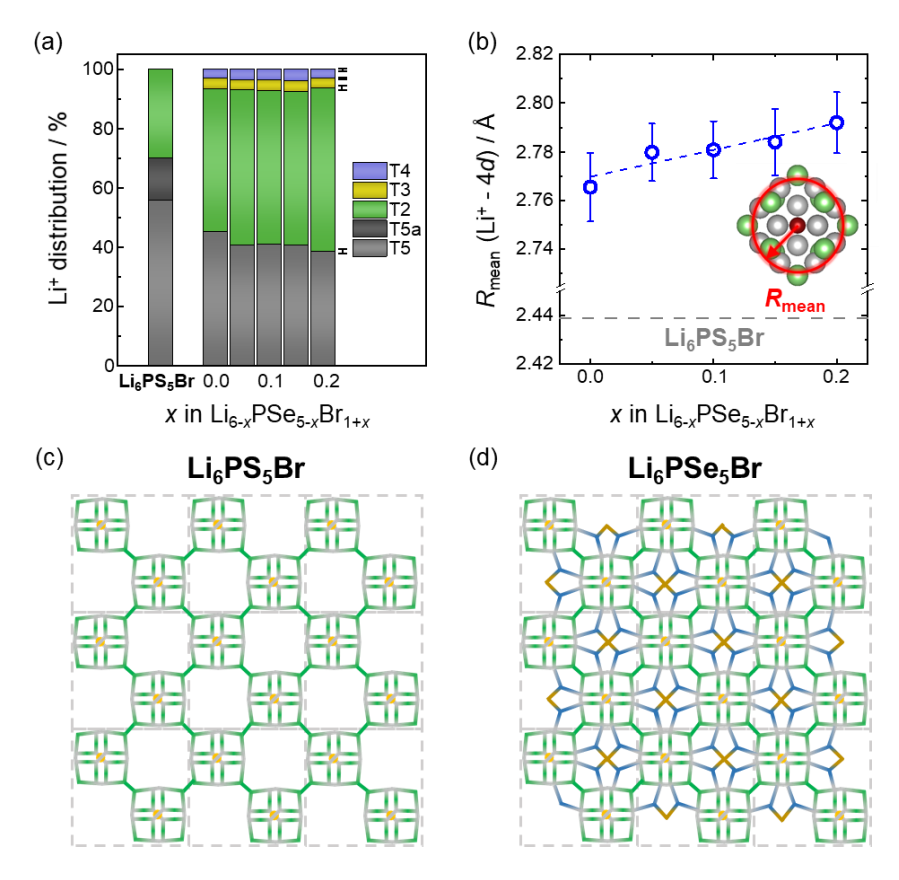


Figure 3. (a) Li⁺ distribution across Li⁺ positions in Li₆PS₅Br and Li_{6-x}PSe_{5-x}Br_{1+x} as a function of x. (b) Mean distance of lithium ions to the Li⁺ cage center (Wyckoff 4d) as a function of x. All uncertainties correspond to one standard deviation based on the refinement of the neutron powder diffraction data. (c) Representation of the connectivity of Li⁺ cages in the case of Li₆PS₅Br including T5 and T5a sites (grey) and T2 sites (green). (d) Representation of the

connectivity of Li⁺ cages in the case of Li₆PSe₅Br including T5 and T5a sites (grey), T2 sites (green), T3 sites (orange) and T4 sites (blue).

Using temperature dependent powder neutron diffraction, changes of the Li⁺ site-occupancy with temperature have been investigated between 150 K and 293 K for Li₆PSe₅Br and Li_{5.85}PSe_{4.85}Br_{1.15} and are compared to Li₆PS₅Br. While the trend is not as pronounced as for Li₆PS₅Br, also the selenophosphates show a tendency towards decreasing occupancy on the T5 position with increasing temperature (Figure S10). These results suggest, that while the T5 position may still be the energetically lowest position on the potential energy surface of all occupied Li⁺ positions, the other Li⁺ positions are very similar in terms of their potential energy.

As the mean distances of lithium ions to the center of the Li⁺ cages formed around Wyckoff-4d, named R_{mean} , has been shown to be a valuable descriptor of the changing Li⁺ substructure in lithium argyrodites²³, Figure 3b shows this for the series of solid solutions Li_{6-x}PSe_{5-x}Br_{1+x} which reveals an expansion of the Li⁺ cages with increasing bromide content. This observation is analogous to the Li_{6-x}PS_{5-x}Cl_{1+x} substitution series, in which a cage expansion was observed for higher x and was correlated to lowering of the effective anionic charge in the cage center due to substitution of S²⁻ by Cl⁻.²⁸

Ionic transport. Temperature dependent electrochemical impedance spectroscopy was employed to measure the ionic conductivity and activation energies for ionic transport for $\text{Li}_{6-x}\text{PSe}_{5-x}\text{Br}_{1+x}$ ($0 \le x \le 0.2$). To minimize uncertainties of the extracted impedance values caused by the high ionic conductivity of the materials, low-temperature impedance data was acquired from 173 K to 298 K.

The impedance spectra recorded at temperatures from 173 K to 298 K were fit with an equivalent circuit model containing a resistor in series with a constant phase element (CPE) corresponding to the materials total resistance and the electrode blocking behavior respectively (Figure 4a,b). More complex models give unreasonable fits at these temperatures, as the processes cannot be further resolved. At lower temperatures from 173 K to 213 K, it was possible to fit the data with an equivalent circuit model consisting of two serial elements containing a resistor in parallel to a CPE, in series with another CPE (Figure S11). The resulting fits are in good agreement with the obtained experimental data as it is exemplary shown for Li₆PSe₅Br in Figure 4c. For the first RP element capacitances around 4 · 10⁻¹¹ F suggest this process is related to bulk transport. Alpha values of 0.97 demonstrate the ideality of the semicircle. ⁴⁷ For the second RP element, capacitances between 3 · 10⁻⁹ to 8 · 10⁻⁹ F indicate the corresponding semicircle may be attributed to the grain boundaries.⁴⁸ However, low alpha values between 0.5 to 0.65 provide indication that the grain boundary contributions cannot be clearly deconvoluted, as it is typical for lithium argyrodites. ⁴⁹ Therefore, for further calculations only the total resistance is considered. The calculated temperature dependent ionic conductivities exhibit linear Arrhenius behavior as shown in Figure 4d.

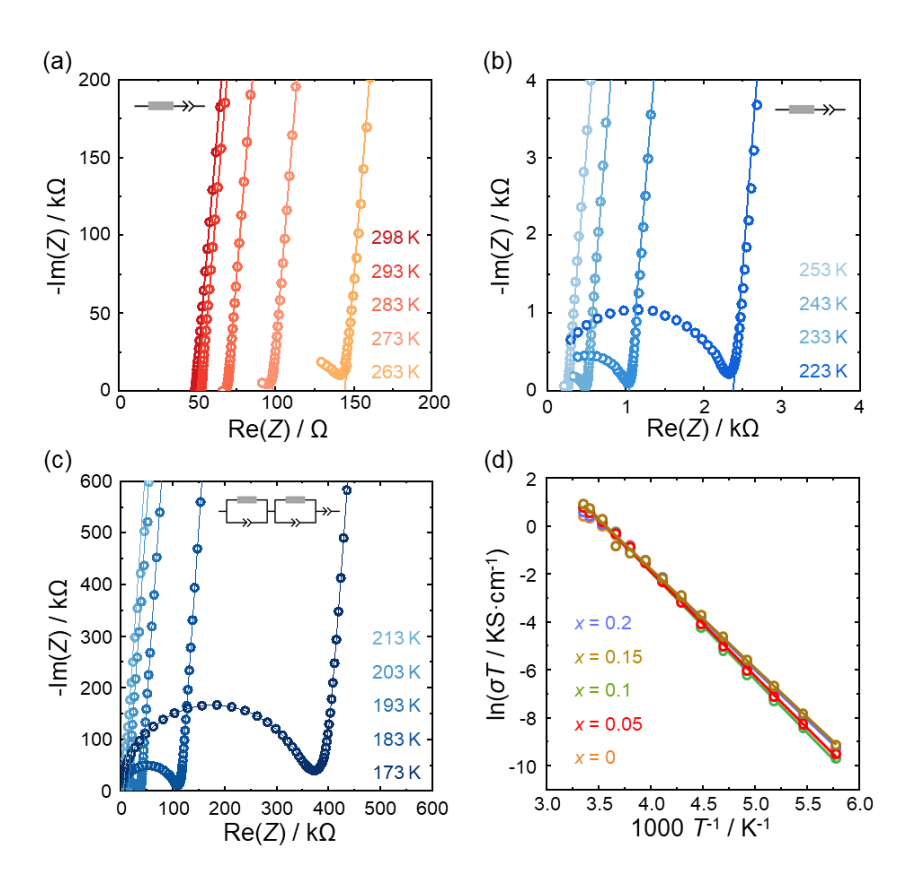


Figure 4. (a) Arrhenius plots of the $Li_{6-x}PSe_{5-x}Cl_{1+x}$ solid solution. (b)-(d) Representative Nyquist plots for temperature dependent impedance data of Li_6PSe_5Br . Insets show the equivalent circuit models used to fit the impedance data.

Figure 5a shows the evolution of ionic conductivity with changing composition. Already for pristine $\text{Li}_6\text{PS}_5\text{Br}$ the ionic conductivity is significantly higher than compared to $\text{Li}_6\text{PS}_5\text{Br}$, reaching 5.0 mS·cm⁻¹, which is likely a result of the better interconnection of the Li⁺ cages along with increasing unit cell volume and lattice softening. With increasing bromide content an increase in ionic conductivity up to a maximum of 8.5 mS·cm⁻¹ at x=0.15 was measured. The trends in ionic conductivity can be correlated to the evolution of R_{mean} , with further displacement of lithium ions away from the cage center leading to higher ionic conductivities (Figure 5b), promoting an even better interconnection of Li^+ cages. For the composition x=0.2 the conductivity drops, although the solubility limit may have not yet been reached based on the diffraction. At this stage, two possible explanations seem reasonable: 1) while the solubility limit has not been reached based on diffraction, LiBr exsolution may have already started (see Figure S3) or 2) the lower conductivity may be due to the adjusted sintering conditions for x=0.2 as a high mechanical fragility was observed. The changing mechanical properties or thermal treatment history, which has been shown to affect the ionic conductivity, 33 can affect transport.

The activation energies show values between 0.35 and 0.39 eV determined by impedance spectroscopy and 0.25 and 0.26 eV determined by ⁷Li NMR spin-lattice relaxometry across all compositions, which is in line with the observed high Li⁺ conductivities. The deviations in the

activation energies are related to the intrinsic differences between ⁷Li NMR relaxometry and impedance spectroscopy. ⁷Li NMR relaxometry mainly considers the activation energy related to ionic transport through the bulk of the material, while the contributions of ionic jumps over grain boundaries can be neglected. ⁵⁰ The fitted ⁷Li relaxometry NMR data is given for Li₆PSe₅Br in Figure 5c and for all remaining compositions in Figure S12.

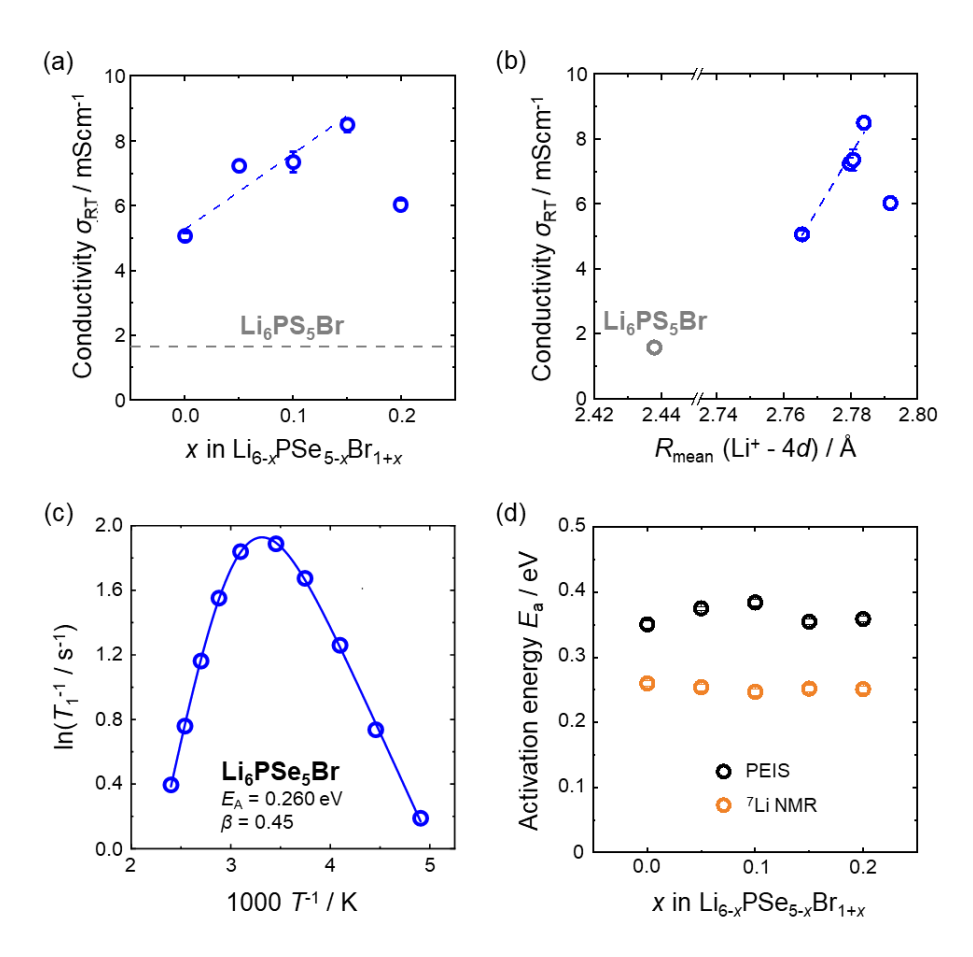


Figure 5. Room temperature ionic conductivities as a function of (a) composition and (b) R_{mean} . (c) Arrhenius plot of the 7 Li NMR spin-lattice relaxation rates for Li_6PSe_5Br with indicated Li^+ self-diffusion activation energy E_a (see also Figure S12). β denotes a stretching exponent from a modified BBP fit (see in reference for details). 50 (d) Activation energies determined by potentiostatic electrochemical impedance spectroscopy and 7Li NMR relaxometry. Note that the error bars are enclosed within the symbols.

Evaluation of the selenophosphates as catholytes. Due to their high ionic conductivities the materials from the Li_{6-x}PSe_{5-x}Br_{1+x} substitution series appear as promising candidates for catholytes in solid-state batteries. In order to verify their performance, the highest conducting composition of the solid solution series Li_{5.85}PSe_{4.85}Br_{1.15} is tested as catholyte in In/LiIn|Li₆PS₅Br|NCM-83:Li_{5.85}PSe_{4.85}Br_{1.15} half-cells and compared to Li₆PS₅Br as a catholyte.

for In Figure 6a the cycling data the first ten cycles of In/LiIn|Li₆PS₅Br|NCM-83:Li_{5.85}PSe_{4.85}Br_{1.15} cell in a potential range of 2.0 – 3.7 V versus In/LiIn and with a charging rate of 0.1 C (areal capacity $q_a = 1.65$ mAh·cm⁻² and current density $i = 0.165 \text{ mA} \cdot \text{cm}^{-2}$) is shown. For comparison, the first ten In/LiIn|Li₆PS₅Br|NCM-83:Li₆PS₅Br cell using Li₆PS₅Br instead of Li_{5.85}PSe_{4.85}Br_{1.15} as catholyte at the same charging rate of 0.1 C ($q_a = 1.99 \text{ mAh} \cdot \text{cm}^{-2}$, $j = 0.199 \text{ mA} \cdot \text{cm}^{-2}$) is given in Figure 6b. The reference cell with NCM-83:Li₆PS₅Br cathode composite achieves a high initial charge capacity of 208 mAh·g⁻¹ and high charge and discharge capacities around 150 mAh·g⁻¹ in subsequent cycles. In contrast, the cell with NCM-83:Li_{5.85}PSe_{4.85}Br_{1.15} cathode composite only achieves a low initial charge capacity of 39 mAh·g⁻¹ and negligible charge and discharge capacities in the subsequent cycles. Additionally, the typical features of a charging curve as it can be seen for In/LiIn|Li₆PS₅Br|NCM-83:Li₆PS₅Br cells in Figure 6b are not present. The impedance data collected after each charge are shown for the 1st, 2nd, 3rd, 5th and 10th cycle of both cells in Figure 6c and 6d. While the impedance data for the reference cell suggest only a slight increase of total impedance from the 1st to the 10th cycle from around 200 Ω to 300 Ω , the total impedance of the cell with the Li_{5.85}PSe_{4.85}Br_{1.15} catholyte shows very high total resistances of over 40 k Ω , even after the first cycle.

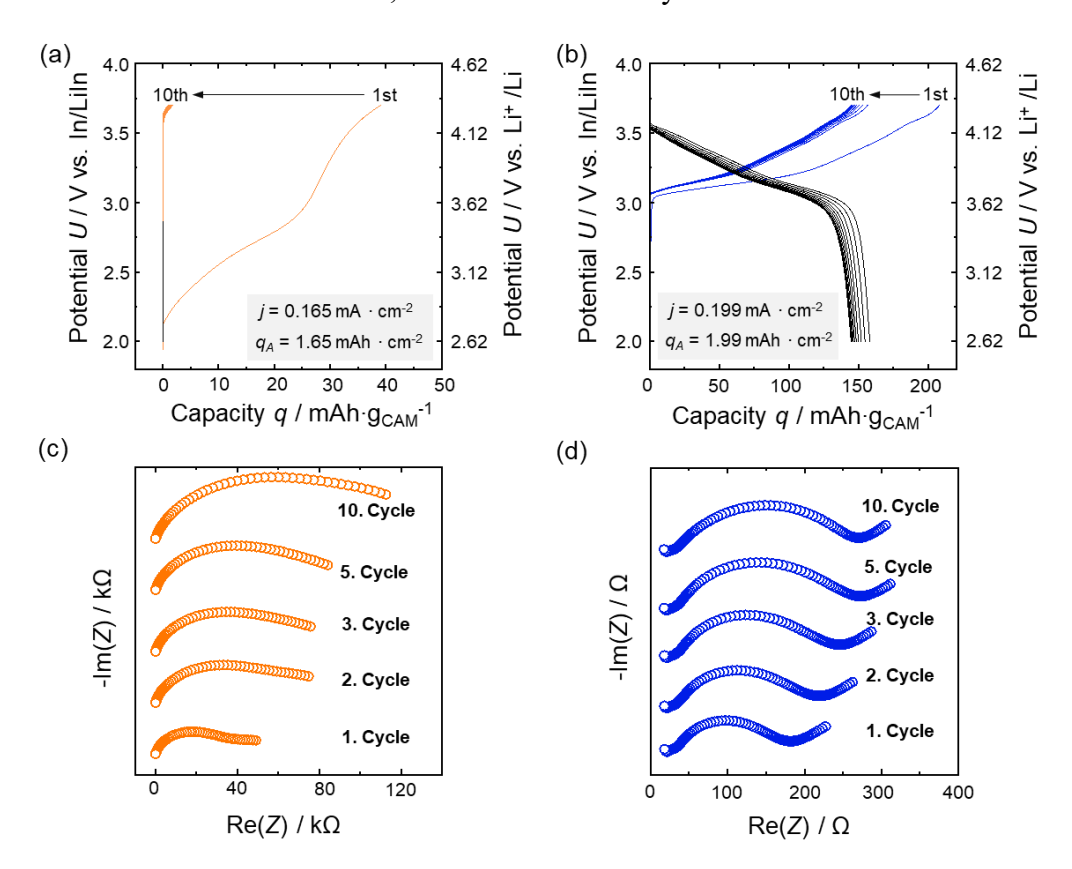


Figure 6. (a), (b) Charge and discharge curves of the first ten cycles of an In/LiIn/Li₆PS₅Br/NCM-83:SE cell at 0.1 C and 25°C containing Li₆PS₅Br (orange) or Li₆PS₅Br (blue) as catholyte. (c), (d) Evolution of total impedance after charging during the first ten cycles of an In/LiIn/Li₆PS₅Br/NCM-83:SE cell at 0.1 C and 25°C containing Li₆PS₅Br

(orange) or Li_6PS_5Br (blue) as catholyte. Due to the shifting of the impedances, the y-axis scales are arbitrary and are hence omitted.

To investigate the chemical stability of Li_{5.85}PSe_{4.85}Br_{1.15} against NCM-83 at room temperature, an In/LiIn|Li₆PS₅Br|NCM-83:Li_{5.85}PSe_{4.85}Br_{1.15} cell was kept at open circuit voltage (OCV) without cycling. Impedance spectra recorded after 6 h and 54 h of OCV show unchanged low total resistances of these cells, indicating chemical stability under these conditions (Figure S13). These results suggest that the severe decomposition in the first charge cycle, is a result of the electrochemical instability of Li_{5.85}PSe_{4.85}Br_{1.15} at elevated potentials. In a theoretical study on chalcogenide substitutions in lithium argyrodites by Chen *et al.* a smaller band gap and lower structural stability of selenophosphate-based argyrodites compared to their sulfide-based counterpart has been reported.⁵¹ The smaller electrochemical stability window likely makes selenophosphate-based argyrodites more prone to oxidation.

To further investigate the influence of applied potential on the degradation during cycling, recorded after each impedance spectra were 0.2 V charging In/LiIn|Li₆PS₅Br|NCM-83:Li_{5.85}PSe_{4.85}Br_{1.15} cells charged with 0.1 C from 2.0 – 3.7 V vs. In/LiIn (Figure 7). Already at 3.0 V vs. In/LiIn an increase of total resistance was observed, indicating the formation of an resistive interphase. With further increasing voltage, the total resistance grows continuously. Similar experiments were conducted In/LiIn|Li₆PS₅Br|NCM-83:Li₆PS₅Br cells. These cells show an onset of degradation at 3.2 V vs. In/LiIn, but a significantly smaller total resistance of less than 100 Ω at 3.6 V vs. In/LiIn.

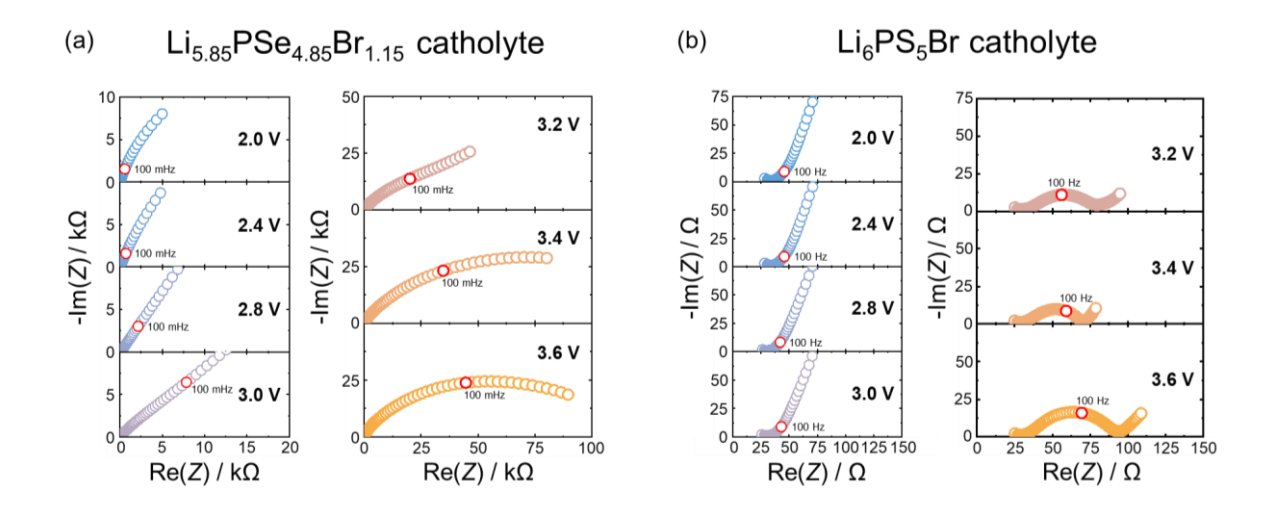


Figure 7: Evolution of total impedance along with increasing potential U vs. In/LiIn in (a) In/LiIn/Li₆PS₅Br/NCM-83:Li_{5.85}PSe_{4.85}Br_{1.15} and (b) In/LiIn/Li₆PS₅Br/NCM-83:Li₆PS₅Br cells. The color gradient from blue to orange emphasizes the increase in potential U from 2.0 V to 3.6 V.

While the onset of degradation at lower potentials against In/LiIn when using Li_{5.85}PSe_{4.85}Br_{1.15} as catholyte may be a result of a smaller electrochemical stability window, the significant

increase in total resistance at higher voltages is likely caused by detrimental properties of the resulting degradation products. 51,52 In sulfide-based lithium argyrodites, degradation phenomena at the interface of NCM and the solid electrolyte have been identified to significantly impede the Coulomb efficiency, due to formation of phosphate and sulfate-like species involving lithium and transition-metal ions as the cationic species.⁵³ The thickness of the interphase layer forming around NCM particles gradually increases during cycling, eventually inhibiting the Li⁺ transport to and from NCM particles during operation of the cell. In the case of selenophosphate-based argyrodites, degradation products based on selenates or selenites are conceivable. In contrast to sulfates, these compounds have significantly smaller band gaps and thus may facilitate electronic transport and thereby faster degradation of the catholyte.54 Further investigation of the decomposition products forming at the interface of NCM-83 and the Li_{5.85}PSe_{4.85}Br_{1.15} by X-ray photoelectrons spectroscopy or comparable techniques have not been conducted, as above cycling experiments clearly show that solid electrolytes of the Li_{6-x}PSe_{5-x}Br_{1+x} substitution series are not suitable for use as catholyte in solid-state batteries, at least when using NCM-based active materials above 3 V versus In/LiIn. In addition to their poor performance as catholytes in SSBs, selenophosphate-based solid electrolytes are concerning from as safety perspective, as exposure to humidity results in the evolution of hazardous H₂Se.⁵⁵ Nevertheless, cycling within a lower voltage range or the use of the material in other cell chemistries such as Li-S batteries is potentially possible, but this requires further investigation. The results of the cycling experiments highlight, that for development of highly conducting solid electrolyte materials, it is crucial to also test the material in cells to ensure chemical and electrochemical stability.

4. Conclusion

In this work, the $\text{Li}_{6-x}\text{PSe}_{5-x}\text{Br}_{1+x}$ ($0 \le x \le 0.2$) substitution series has been explored and the performance of $\text{Li}_{5.85}\text{PSe}_{4.85}\text{Br}_{1.15}$ as catholyte in solid-state batteries has been tested. Using a combination of neutron powder diffraction, $^{31}\text{P-NMR}$ and Raman spectroscopy for structural investigations as well as potentiostatic electrochemical impedance spectroscopy and $^{7}\text{Li NMR}$ relaxometry to probe the Li^{+} transport, structure-transport relationships were unveiled.

High Li⁺ conductivities of 5.0 mS·cm⁻¹ for Li₆PSe₅Br up to 8.5 mS·cm⁻¹ were found in the Li_{6-x}PSe_{5-x}Br_{1+x} ($0 \le x \le 0.2$) substitution series. Comparing Li₆PSe₅Br with its thiophosphate analogue reveals the occupation of two additional Li⁺ positions T3 and T4, opening up further diffusion pathways and thereby providing better interconnection of the Li⁺ cages in selenophosphate-based lithium argyrodites. Additionally, larger lattice parameters and a softening of the lattice upon introduction of selenium were discovered. The increase of ionic conductivity at higher degree of substitution x in Li_{6-x}PSe_{5-x}Br_{1+x} ($0 \le x \le 0.15$) could be correlated with the increase of the mean distance of Li⁺ ions to the center of the Li⁺ cages R_{mean} and higher Li⁺ occupancy on positions involved in inter-cage transport. Solid-state batteries

using Li_{5.85}PSe_{4.85}Br_{1.15} as catholytes indicate the formation of a highly resistive interphase at potentials \geq 3 V vs. In/LiIn. This finding suggests that, together with the higher toxicity of H₂Se, selenophosphate-based materials are not suitable for application in solid-state batteries that use NCM as active materials, nevertheless the high ionic conductivities may be interesting for conversion-type active materials such Si, FeS₂ or S.

Besides expanding on the understanding of the structure-transport relationship in lithium argyrodites, this work demonstrates that good chemical and electrochemical stability of electrolyte materials are indispensable for the construction of solid-state batteries with high performance and long cycle life.

Supporting Information

The supporting information is available free of charge at [link].

Illustration of type 1 to type 5 tetrahedral voids in lithium argyrodites, neutron diffraction data, refined lithium bromide side phase content, Rietveld refinement results including tabulated constraints and structural data, ³¹P MAS NMR spectra, illustration of the coordination spheres of phosphorous, comparison of integrated ³¹P MAS NMR intensities to statistical mixing, Raman spectra, temperature dependent Li⁺ distribution, fitting of low temperature impedance data, Arrhenius plots of the ⁷Li NMR spin-lattice relaxation rates and temporal impedance evolution of In/LiIn|Li₆PS₅Br|NCM-83/Li_{5.85}PSe_{4.85}Br_{1.15} cells at OCV (PDF)

Crystallographic information files (ZIP)

Acknowledgements

The authors acknowledge financial support within the cluster of competence FESTBATT funded by the Bundesministerium für Bildung und Forschung (BMBF; project 03XP0430F). B.W. is member of the International Graduate School for Battery Chemistry, Characterization, Analysis, Recycling and Application (BACCARA), which is funded by the Ministry for Culture and Science of North Rhine-Westphalia, Germany. A portion of this research used resources at the Spallation Neutron Source, a DOE Office of Science User Facility operated by the Oak Ridge National Laboratory.

Conflict of interests

The authors declare no conflict of interest.

References

- (1) Randau, S.; Weber, D. A.; Kötz, O.; Koerver, R.; Braun, P.; Weber, A.; Ivers-Tiffée, E.; Adermann, T.; Kulisch, J.; Zeier, W. G.; Richter, F. H.; Janek, J. Benchmarking the Performance of All-Solid-State Lithium Batteries. *Nat. Energy* **2020**, *5*, 259–270. https://doi.org/10.1038/s41560-020-0565-1.
- (2) Janek, J.; Zeier, W. G. A Solid Future for Battery Development. *Nat. Energy* **2016**, *1*, No. 16141. https://doi.org/10.1038/nenergy.2016.141.
- (3) Manthiram, A.; Yu, X.; Wang, S. Lithium Battery Chemistries Enabled by Solid-State Electrolytes. *Nat. Rev. Mater* **2017**, *2*, 1–16. https://doi.org/10.1038/natrevmats.2016.103.
- (4) Minnmann, P.; Quillman, L.; Burkhardt, S.; Richter, F. H.; Janek, J. Quantifying the Impact of Charge Transport Bottlenecks in Composite Cathodes of All-Solid-State Batteries. *J. Electrochem. Soc.* **2021**, *168*, No. 040537. https://doi.org/10.1149/1945-7111/abf8d7.
- (5) Janek, J.; Zeier, W. G. Challenges in Speeding up Solid-State Battery Development. *Nat. Energy* **2023**, *3*, 230-240. https://doi.org/10.1038/s41560-023-01208-9.
- (6) Dewald, G. F.; Ohno, S.; Hering, J. G. C.; Janek, J.; Zeier, W. G. Analysis of Charge Carrier Transport Toward Optimized Cathode Composites for All-Solid-State Li-S Batteries. *Batter. Supercaps* **2021**, *4*, 183–194. https://doi.org/10.1002/batt.202000194.
- (7) Ohno, S.; Rosenbach, C.; Dewald, G. F.; Janek, J.; Zeier, W. G. Linking Solid Electrolyte Degradation to Charge Carrier Transport in the Thiophosphate-Based Composite Cathode toward Solid-State Lithium-Sulfur Batteries. *Adv. Funct. Mater.* **2021**, *31*, No. 2010620. https://doi.org/10.1002/adfm.202010620.
- (8) Kato, Y.; Shiotani, S.; Morita, K.; Suzuki, K.; Hirayama, M.; Kanno, R. All-Solid-State Batteries with Thick Electrode Configurations. *J. Phys. Chem. Lett.* 2018, 9, 607–613. https://doi.org/10.1021/acs.jpclett.7b02880.
- (9) Fu, K.; Gong, Y.; Hitz, G. T.; McOwen, D. W.; Li, Y.; Xu, S.; Wen, Y.; Zhang, L.; Wang, C.; Pastel, G.; Dai, J.; Liu, B.; Xie, H.; Yao, Y.; Wachsman, E. D.; Hu, L. Three-Dimensional Bilayer Garnet Solid Electrolyte Based High Energy Density Lithium Metal—Sulfur Batteries. *Energy Environ. Sci.* 2017, 10, 1568–1575. https://doi.org/10.1039/c7ee01004d.
- (10) Jiang, T.; He, P.; Wang, G.; Shen, Y.; Nan, C. W.; Fan, L. Z. Solvent-Free Synthesis of Thin, Flexible, Nonflammable Garnet-Based Composite Solid Electrolyte for All-Solid-State Lithium Batteries. *Adv. Energy Mater.* **2020**, *10*, No. 1903376. https://doi.org/10.1002/aenm.201903376.
- (11) Li, X.; Liang, J.; Luo, J.; Norouzi Banis, M.; Wang, C.; Li, W.; Deng, S.; Yu, C.; Zhao, F.; Hu, Y.; Sham, T. K.; Zhang, L.; Zhao, S.; Lu, S.; Huang, H.; Li, R.; Adair, K. R.; Sun, X. Air-Stable Li₃InCl₆ Electrolyte with High Voltage Compatibility for All-Solid-State Batteries. *Energy Environ. Sci.* **2019**, *12*, 2665−2671. https://doi.org/10.1039/c9ee02311a.
- (12) Kwak, H.; Han, D.; Lyoo, J.; Park, J.; Jung, S. H.; Han, Y.; Kwon, G.; Kim, H.; Hong, S. T.; Nam, K. W.; Jung, Y. S. New Cost-Effective Halide Solid Electrolytes for All-Solid-State Batteries: Mechanochemically Prepared Fe³⁺-Substituted Li₂ZrCl₆. *Adv. Energy Mater.* **2021**, *11*, No. 2003190. https://doi.org/10.1002/aenm.202003190.
- (13) Li, X.; Liang, J.; Chen, N.; Luo, J.; Adair, K. R.; Wang, C.; Banis, M. N.; Sham, T. K.; Zhang, L.; Zhao, S.; Lu, S.; Huang, H.; Li, R.; Sun, X. Water-Mediated Synthesis of a Superionic Halide Solid

- Electrolyte. *Angew. Chem. Int. Ed.* **2019**, *58*, 16427–16432. https://doi.org/10.1002/ange.201909805.
- (14) Zallocco, V. M.; Freitas, J. M.; Bocchi, N.; Rodrigues, A. C. M. Electrochemical Stability of a NASICON Solid Electrolyte from the Lithium Aluminum Germanium Phosphate (LAGP) Series. Solid State Ion. 2022, 378, No. 115888. https://doi.org/10.1016/j.ssi.2022.115888.
- (15) Liu, Y.; Chen, J.; Gao, J. Preparation and Chemical Compatibility of Lithium Aluminum Germanium Phosphate Solid Electrolyte. *Solid State Ion.* **2018**, *318*, 27–34. https://doi.org/10.1016/j.ssi.2017.10.016.
- (16) Yoshinari, T.; Koerver, R.; Hofmann, P.; Uchimoto, Y.; Zeier, W. G.; Janek, J. Interfacial Stability of Phosphate-NASICON Solid Electrolytes in Ni-Rich NCM Cathode-Based Solid-State Batteries. *ACS Appl. Mater. Interfaces* **2019**, *11*, 23244–23253. https://doi.org/10.1021/acsami.9b05995.
- (17) Kraft, M. A.; Ohno, S.; Zinkevich, T.; Koerver, R.; Culver, S. P.; Fuchs, T.; Senyshyn, A.; Indris, S.; Morgan, B. J.; Zeier, W. G. Inducing High Ionic Conductivity in the Lithium Superionic Argyrodites Li_{6+x}P_{1-x}Ge_xS₅I for All-Solid-State Batteries. *J. Am. Chem. Soc.* **2018**, *140*, 16330-16339. https://doi.org/10.1021/jacs.8b10282.
- (18) Adeli, P.; Bazak, J. D.; Park, K. H.; Kochetkov, I.; Huq, A.; Goward, G. R.; Nazar, L. F. Boosting Solid-State Diffusivity and Conductivity in Lithium Superionic Argyrodites by Halide Substitution. *Angew. Chem. Int. Ed.* **2019**, *58*, 8681–8686. https://doi.org/10.1002/anie.201814222.
- (19) Murayama, M.; Kanno, R.; Irie, M.; Ito, S.; Hata, T.; Sonoyama, N.; Kawamoto, Y. Synthesis of New Lithium Ionic Conductor Thio-LISICON Lithium Silicon Sulfides System. *J. Solid State Chem.* **2002**, *168*, 140–148. https://doi.org/10.1006/jssc.2002.9701.
- (20) Dietrich, C.; Weber, D. A.; Sedlmaier, S. J.; Indris, S.; Culver, S. P.; Walter, D.; Janek, J.; Zeier, W. G. Lithium Ion Conductivity in Li₂S–P₂S₅ Glasses Building Units and Local Structure Evolution during the Crystallization of Superionic Conductors Li₃PS₄, Li₇P₃S₁₁ and Li₄P₂S₇. *J. Mater. Chem. A Mater.* **2017**, *5*, 18111–18119. https://doi.org/10.1039/C7TA06067J.
- (21) Kuhn, A.; Gerbig, O.; Zhu, C.; Falkenberg, F.; Maier, J.; Lotsch, B. V. A New Ultrafast Superionic Li-Conductor: Ion Dynamics in Li₁₁Si₂PS₁₂ and Comparison with Other Tetragonal LGPS-Type Electrolytes. *Phys. Chem. Chem. Phys.* **2014**, *16*, 14669–14674. https://doi.org/10.1039/c4cp02046d.
- (22) Sakuda, A.; Hayashi, A.; Tatsumisago, M. Sulfide Solid Electrolyte with Favorable Mechanical Property for All-Solid-State Lithium Battery. *Sci. Rep.* **2013**, *3*, No. 2261. https://doi.org/10.1038/srep02261.
- (23) Zhou, L.; Minafra, N.; Zeier, W. G.; Nazar, L. F. Innovative Approaches to Li-Argyrodite Solid Electrolytes for All-Solid-State Lithium Batteries. *Acc. Chem. Res.* **2021**, *54*, 2717–2728. https://doi.org/10.1021/acs.accounts.0c00874.
- (24) Zhou, L.; Assoud, A.; Zhang, Q.; Wu, X.; Nazar, L. F. New Family of Argyrodite Thioantimonate Lithium Superionic Conductors. J. Am. Chem. Soc. 2019, 141, 19002–19013. https://doi.org/10.1021/jacs.9b08357.
- (25) Patel, S. V.; Banerjee, S.; Liu, H.; Wang, P.; Chien, P. H.; Feng, X.; Liu, J.; Ong, S. P.; Hu, Y. Y. Tunable Lithium-Ion Transport in Mixed-Halide Argyrodites Li_{6-x}PS_{5-x}ClBr_x: An Unusual

- Compositional Space. *Chem. Mater.* **2021**, *33*, 1435–1443. https://doi.org/10.1021/acs.chemmater.0c04650.
- (26) Wang, P.; Liu, H.; Patel, S.; Feng, X.; Chien, P. H.; Wang, Y.; Hu, Y. Y. Fast Ion Conduction and Its Origin in Li_{6-x}PS_{5-x}Br_{1+x}. *Chem. Mater.* **2020**, *32*, 3833–3840. https://doi.org/10.1021/acs.chemmater.9b05331.
- (27) Bielefeld, A.; Weber, D. A.; Janek, J. Modeling Effective Ionic Conductivity and Binder Influence in Composite Cathodes for All-Solid-State Batteries. *ACS Appl. Mater. Interfaces* **2020**, *12*, 12821–12833. https://doi.org/10.1021/acsami.9b22788.
- (28) Gautam, A.; Ghidiu, M.; Suard, E.; Kraft, M. A.; Zeier, W. G. On the Lithium Distribution in Halide Superionic Argyrodites by Halide Incorporation in Li_{7-x}PS_{6-x}Cl_x. *ACS Appl. Energy Mater.* **2021**, *4*, 7309–7315. https://doi.org/10.1021/acsaem.1c01417.
- (29) Deiseroth, H. J.; Maier, J.; Weichert, K.; Nickel, V.; Kong, S. T.; Reiner, C. Li₇PS₆ and Li₆PS₅X (X: Cl, Br, I): Possible Three-Dimensional Diffusion Pathways for Lithium Ions and Temperature Dependence of the Ionic Conductivity by Impedance Measurements. *Z. Anorg. Allg. Chem.* **2011**, *637*, 1287–1294. https://doi.org/10.1002/zaac.201100158.
- (30) Deiseroth, H. J.; Kong, S. T.; Eckert, H.; Vannahme, J.; Reiner, C.; Zaiß, T.; Schlosser, M. Li₆PS₅X: A Class of Crystalline Li-Rich Solids with an Unusually High Li⁺ Mobility. *Angew. Chem. Int. Ed.* 2008, 47, 755−758. https://doi.org/10.1002/anie.200703900.
- (31) Kong, S. T.; Deiseroth, H. J.; Reiner, C.; Gün, Ö.; Neumann, E.; Ritter, C.; Zahn, D. Lithium Argyrodites with Phosphorus and Arsenic: Order and Disorder of Lithium Atoms, Crystal Chemistry, and Phase Transitions. *Chem. Eur. J* **2010**, *16*, 2198–2206. https://doi.org/10.1002/chem.200902470.
- (32) Kraft, M. A.; Culver, S. P.; Calderon, M.; Böcher, F.; Krauskopf, T.; Senyshyn, A.; Dietrich, C.; Zevalkink, A.; Janek, J.; Zeier, W. G. Influence of Lattice Polarizability on the Ionic Conductivity in the Lithium Superionic Argyrodites Li₆PS₅X (X = Cl, Br, I). *J. Am. Chem. Soc.* **2017**, *139*, 10909−10918. https://doi.org/10.1021/jacs.7b06327.
- (33) Gautam, A.; Sadowski, M.; Ghidiu, M.; Minafra, N.; Senyshyn, A.; Albe, K.; Zeier, W. G. Engineering the Site-Disorder and Lithium Distribution in the Lithium Superionic Argyrodite Li₆PS₅Br. *Adv. Energy Mater.* **2021**, *11*, No. 2003369. https://doi.org/10.1002/aenm.202003369.
- (34) Gautam, A.; Sadowski, M.; Prinz, N.; Eickhoff, H.; Minafra, N.; Ghidiu, M.; Culver, S. P.; Albe, K.; Fässler, T. F.; Zobel, M.; Zeier, W. G. Rapid Crystallization and Kinetic Freezing of Site-Disorder in the Lithium Superionic Argyrodite Li₆PS₅Br. *Chem. Mater.* **2019**, *31*, 10178−10185. https://doi.org/10.1021/acs.chemmater.9b03852.
- (35) Hogrefe, K.; Minafra, N.; Hanghofer, I.; Banik, A.; Zeier, W. G.; Wilkening, H. M. R. Opening Diffusion Pathways through Site Disorder: The Interplay of Local Structure and Ion Dynamics in the Solid Electrolyte Li_{6+x}P_{1-x}Ge_xS₅I as Probed by Neutron Diffraction and NMR. *J. Am. Chem. Soc.* **2022**, *144*, 1795–1812. https://doi.org/10.1021/jacs.1c11571.
- (36) Stamminger, A. R.; Ziebarth, B.; Mrovec, M.; Hammerschmidt, T.; Drautz, R. Ionic Conductivity and Its Dependence on Structural Disorder in Halogenated Argyrodites Li_6PS_5X (X = Br, Cl, I). *Chem. Mater.* **2019**, *31*, 8673–8678. https://doi.org/10.1021/acs.chemmater.9b02047.

- (37) Minafra, N.; Kraft, M. A.; Bernges, T.; Li, C.; Schlem, R.; Morgan, B. J.; Zeier, W. G. Local Charge Inhomogeneity and Lithium Distribution in the Superionic Argyrodites Li₆PS₅X (X = Cl, Br, I).

 Inorg. Chem. **2020**, *59*, 11009−11019. https://doi.org/10.1021/acs.inorgchem.0c01504.
- (38) Morgan, B. J. Mechanistic Origin of Superionic Lithium Diffusion in Anion-Disordered Li₆PS₅X Argyrodites. *Chem. Mater.* **2021**, *33*, 2004–2018. https://doi.org/10.1021/acs.chemmater.0c03738.
- (39) De Klerk, N. J. J.; Rosłoń, I.; Wagemaker, M. Diffusion Mechanism of Li Argyrodite Solid Electrolytes for Li-Ion Batteries and Prediction of Optimized Halogen Doping: The Effect of Li Vacancies, Halogens, and Halogen Disorder. *Chem. Mater.* **2016**, *28*, 7955–7963. https://doi.org/10.1021/acs.chemmater.6b03630.
- (40) Bernges, T.; Culver, S. P.; Minafra, N.; Koerver, R.; Zeier, W. G. Competing Structural Influences in the Li Superionic Conducting Argyrodites $Li_6PS_{5-x}Se_xBr$ ($0 \le x \le 1$) upon Se Substitution. *Inorg. Chem.* **2018**, *57*, 13920–13928. https://doi.org/10.1021/acs.inorgchem.8b02443.
- (41) Schlem, R.; Ghidiu, M.; Culver, S. P.; Hansen, A. L.; Zeier, W. G. Changing the Static and Dynamic Lattice Effects for the Improvement of the Ionic Transport Properties within the Argyrodite Li₆PS_{5-x}Se_xI. *ACS Appl. Energy Mater.* **2020**, *3*, 9–18. https://doi.org/10.1021/acsaem.9b01794.
- (42) Huq, A.; Kirkham, M.; Peterson, P. F.; Hodges, J. P.; Whitfield, P. S.; Page, K.; Hűgle, T.; Iverson, E. B.; Parizzi, A.; Rennich, G. POWGEN: Rebuild of a Third-Generation Powder Diffractometer at the Spallation Neutron Source. *J. Appl. Crystallogr.* 2019, 52, 1189–1201. https://doi.org/10.1107/S160057671901121X.
- (43) Van Geet, A. L. Calibration of the Methanol and Glycol Nuclear Magnetic Resonance Thermometers with a Static Thermistor Probe. *Anal. Chem.* **1968**, *40*, 2227–2229.
- (44) Zhang, W.; Weber, D. A.; Weigand, H.; Arlt, T.; Manke, I.; Schröder, D.; Koerver, R.; Leichtweiss, T.; Hartmann, P.; Zeier, W. G.; Janek, J. Interfacial Processes and Influence of Composite Cathode Microstructure Controlling the Performance of All-Solid-State Lithium Batteries. ACS Appl. Mater. Interfaces 2017, 9, 17835–17845. https://doi.org/10.1021/acsami.7b01137.
- (45) Shannon, R. D.; Prewitt, C. T. Revised Values of Effective Ionic Radii. *Acta Crystallogr. B* **1970**, *26*, 1046–1048. https://doi.org/10.1107/S0567740870003576.
- (46) Koch, B.; Kong, S. T.; Gün, Ö.; Deiseroth, H. J.; Eckert, H. Site Preferences and Ion Dynamics in Lithium Chalcohalide Solid Solutions with Argyrodite Structure: II. Multinuclear Solid State NMR of the Systems Li₆PS_{5-x}Se_xCl and Li₆PS_{5-x}Se_xBr. *Zeitschrift fuer Physikalische Chemie* **2022**, 236, 875–898. https://doi.org/10.1515/zpch-2021-3139.
- (47) Brug, G. J.; van den Eeden, A. L. G.; Sluyters-Rehbach, M.; Sluyters, J. H. The Analysis of Electrode Impedances Complicated by the Presence of a Constant Phase Element. *J. Electroanal. Chem. Interfacial Electrochem.* **1984**, *176*, 275–295. https://doi.org/10.1016/S0022-0728(84)80324-1.
- (48) Irvine, J. T. S.; Sinclair, D. C.; West, A. R. Electroceramics: Characterization by Impedance Spectroscopy. *Adv. Mater.* **1990**, *2*, 132–138. https://doi.org/10.1002/adma.19900020304.

- (49) Ohno, S.; Bernges, T.; Buchheim, J.; Duchardt, M.; Hatz, A. K.; Kraft, M. A.; Kwak, H.; Santhosha, A. L.; Liu, Z.; Minafra, N.; Tsuji, F.; Sakuda, A.; Schlem, R.; Xiong, S.; Zhang, Z.; Adelhelm, P.; Chen, H.; Hayashi, A.; Jung, Y. S.; Lotsch, B. V.; Roling, B.; Vargas-Barbosa, N. M.; Zeier, W. G. How Certain Are the Reported Ionic Conductivities of Thiophosphate-Based Solid Electrolytes? An Interlaboratory Study. *ACS Energy Lett.* **2020**, *5*, 910–915. https://doi.org/10.1021/acsenergylett.9b02764.
- (50) Wankmiller, B.; Hansen, M. R. Observation of Li+ Jumps in Solid Inorganic Electrolytes over a Broad Dynamical Range: A Case Study of the Lithium Phosphidosilicates Li₈SiP₄ and Li₁₄SiP₆. *J Magn. Reson. Open* **2023**, *14*, 100098. https://doi.org/10.1016/j.jmro.2023.100098.
- (51) Chen, H. M.; Maohua, C.; Adams, S. Stability and Ionic Mobility in Argyrodite-Related Lithium-Ion Solid Electrolytes. *Phys. Chem. Chem. Phys.* **2015**, *17*, 16494–16506. https://doi.org/10.1039/c5cp01841b.
- (52) Banik, A.; Liu, Y.; Ohno, S.; Rudel, Y.; Jiménez-Solano, A.; Gloskovskii, A.; Vargas-Barbosa, N. M.; Mo, Y.; Zeier, W. G. Can Substitutions Affect the Oxidative Stability of Lithium Argyrodite Solid Electrolytes? ACS Appl. Energy Mater. 2022, 5, 2045–2053. https://doi.org/10.1021/acsaem.1c03599.
- (53) Walther, F.; Koerver, R.; Fuchs, T.; Ohno, S.; Sann, J.; Rohnke, M.; Zeier, W. G.; Janek, J. Visualization of the Interfacial Decomposition of Composite Cathodes in Argyrodite-Based All-Solid-State Batteries Using Time-of-Flight Secondary-Ion Mass Spectrometry. *Chem. Mater.* 2019, 31, 3745–3755. https://doi.org/10.1021/acs.chemmater.9b00770.
- (54) Jain, A.; Ong, S. P.; Hautier, G.; Chen, W.; Richards, W. D.; Dacek, S.; Cholia, S.; Gunter, D.; Skinner, D.; Ceder, G.; Persson, K. A. The Materials Project: A Materials Genome Approach to Accelerating Materials Innovation. *APL Mater.* **2013**, *1*, No. 011002. https://doi.org/10.1063/1.4812323.
- (55) Kang, X.; Huang, H.; Jiang, C.; Cheng, L.; Sang, Y.; Cai, X.; Dong, Y.; Sun, L.; Wen, X.; Xi, Z. Cysteine-Activated Small-Molecule H₂Se Donors Inspired by Synthetic H₂S Donors. *J. Am. Chem. Soc.* **2022**, *144*, 3957–3967. https://doi.org/10.1021/jacs.1c12006.

For table of contents only

